Am J Transl Res 2026;18(5):3715-3735
www.ajtr.org /ISSN:1943-8141/AJTR0172686

Original Article

Preoperative prediction of early recurrence and microvascular invasion in hepatocellular carcinoma using conventional ultrasound, elastography, and clinical nutritional indicators: a radiomics-based study

Dong Jiang[1*], Dongyu Chen[1*], Yiran Li[1*], Fengfeng Mo[2*]

[1]Department of Ultrasound Diagnosis and Therapy, Eastern Hepatobiliary Surgery Hospital, The Third Affiliated Hospital of Naval Medical University, Shanghai 200438, China; [2]Department of Nutrition and Food Hygiene, Naval Medical University, Shanghai 200433, China. [*]Equal contributors.

Received March 17, 2026; Accepted April 30, 2026; Epub May 15, 2026; Published May 30, 2026

Abstract: Objectives: To develop and validate preoperative models for predicting 1-year recurrence and microvascular invasion (MVI) in hepatocellular carcinoma (HCC) using conventional ultrasound, elastography, and clinical nutritional indicators. Methods: This retrospective study included patients with pathologically confirmed HCC who underwent curative hepatectomy and preoperative conventional ultrasound plus elastography. A total of 619 patients were included in the recurrence analysis, and 581 patients with complete pathological MVI assessment and complete modeling variables were included in the MVI analysis. Clinical, laboratory, nutritional, ultrasound, and elastography data were collected. Radiomics features were extracted from grayscale ultrasound and elastography images after standardized preprocessing and region-of-interest segmentation. Clinical, radiomics, and combined models were developed in the training cohorts and evaluated in the validation cohorts. Results: For 1-year recurrence prediction, the combined model showed the best performance, with area under the curve (AUC) values of 0.675 in the cross-validation set and 0.771 in the independent test set, compared with 0.567 and 0.656 for the clinical model and 0.660 and 0.759 for the radiomics model, respectively. For MVI prediction, the combined model also achieved the best discriminative performance, with AUC values of 0.860 in the cross-validation set and 0.819 in the independent test set, compared with 0.836 and 0.793 for the clinical model and 0.667 and 0.661 for the radiomics model, respectively. Conclusions: A combined model integrating ultrasound-elastography radiomics and clinical nutritional indicators showed favorable performance for preoperative prediction of both 1-year recurrence and MVI in HCC.

Keywords: Hepatocellular carcinoma, ultrasound radiomics, elastography, early recurrence, microvascular invasion, nutritional indicators

Introduction

Hepatocellular carcinoma (HCC) is a leading primary liver malignancy and remains a major contributor to cancer-related death worldwide. Curative hepatectomy is widely used for patients with resectable disease, but postoperative outcomes are highly heterogeneous [1, 2]. Among the factors associated with poor prognosis, early postoperative recurrence and microvascular invasion (MVI) are particularly important because they reflect biologically aggressive tumor behavior and are closely linked to reduced long-term survival [3-6]. Consequently, reliable preoperative identification of patients at high risk for these adverse features is essential for optimizing surgical planning, perioperative management, and follow-up strategies.

Current preoperative risk stratification for HCC still relies largely on serum markers, tumor burden, and postoperative pathological information [7]. Nevertheless, these measures are not sufficient for comprehensive preoperative evaluation. In particular, key adverse features such as MVI are usually confirmed only after resection, which limits their value in presurgical deci-

https://doi.org/10.62347/NODJ7122

sion-making [8]. In addition, routinely available clinical parameters often fail to reflect the full extent of intratumoral complexity and patient-specific biological variation [9, 10]. Radiomics offers a quantitative imaging-based strategy that converts medical images into high-dimensional features and may reveal subtle characteristics related to tumor heterogeneity and the surrounding microenvironment that are not readily appreciable on visual inspection [11, 12]. In the setting of HCC, ultrasound-based radiomics is especially attractive because ultrasound is safe, readily accessible, dynamic, and already integrated into routine perioperative assessment [13-15].

In addition, conventional ultrasound and elastography may provide complementary information [16, 17]. Conventional ultrasound can reflect tumor morphology, margin characteristics, and vascularity, whereas elastography provides quantitative information on tissue stiffness and biomechanical heterogeneity [18]. These imaging features may be associated with invasive growth, stromal remodeling, and microvascular alterations [19, 20]. Besides tumor-related imaging characteristics, host-related factors may also influence HCC progression and postoperative outcomes. Nutritional and inflammatory status, liver functional reserve, and coagulation-related parameters have all been reported to be associated with recurrence and tumor aggressiveness [21-23]. Nutritional indicators such as Subjective Global Assessment (SGA), prognostic nutritional index (PNI), albumin, and the Controlling Nutritional Status (CONUT) score may therefore provide clinically relevant complementary information for risk prediction [24, 25].

Based on these considerations, we conducted a retrospective study to develop and validate preoperative prediction models for two clinically relevant endpoints in HCC, namely recurrence within 1 year after curative hepatectomy and pathological MVI. By integrating routine preoperative conventional ultrasound, elastography-derived radiomics features, and clinical nutritional indicators, we constructed and compared clinical, radiomics, and combined models. We hypothesized that combining imaging-derived heterogeneity with host nutritional status would improve individualized preoperative risk stratification in patients with HCC.

Materials and methods

Study design and patients

This retrospective cohort study was approved by the institutional ethics committee of the Eastern Hepatobiliary Surgery Hospital (approval No. EHBHKY2023-K034-P001). A total of 700 consecutive patients with a preoperative diagnosis of HCC who were evaluated for curative hepatectomy were initially screened. After exclusion of 81 patients for predefined reasons, including non-primary liver malignancies or other malignant tumors, preoperative antitumor treatment, poor image quality precluding region-of-interest delineation, missing key baseline variables, and loss to follow-up or unclear endpoint status, 619 patients with pathologically confirmed HCC were ultimately included in the study (**Figure 1**). All included patients had complete preoperative conventional ultrasound and elastography examinations, as well as available baseline clinical, laboratory, imaging, follow-up, and postoperative pathological data. Two study endpoints were analyzed separately. For prediction of recurrence within 1 year after surgery, the final cohort of 619 patients was allocated into a training cohort (n = 495) and a validation cohort (n = 124) at a ratio of 4:1 using random allocation with verification of baseline comparability; repeated random splitting was performed to minimize potential imbalance between cohorts. For prediction of MVI, 38 of the 619 patients were excluded because of incomplete postoperative pathological MVI assessment and/or missing key modeling variables; the remaining 581 patients constituted the endpoint-specific MVI cohort and were allocated into a training cohort (n = 465) and a validation cohort (n = 116) using the same strategy of random allocation with verification of baseline comparability, with repeated random splitting to minimize potential imbalance. Because the purpose of this split was predictive model development rather than causal comparison between two exposure groups, propensity score matching was not applied. All feature selection, model construction, and hyperparameter optimization procedures were performed exclusively in the training cohort, and the final model performance was subsequently evaluated in the independent validation cohort.

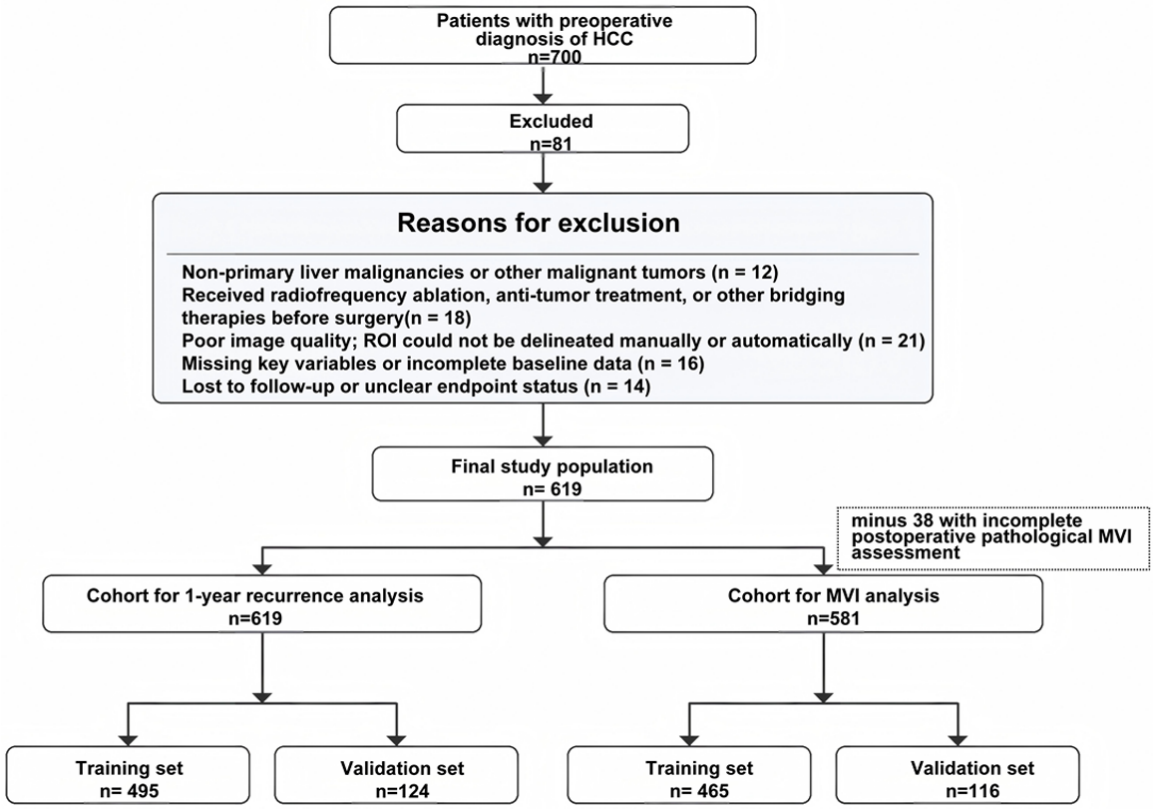

Figure 1. Flowchart of patient selection and cohort allocation for recurrence and microvascular invasion analyses: A total of 619 patients were included in the recurrence analysis. For the MVI analysis, 38 patients were excluded because of incomplete postoperative pathological MVI assessment and/or missing key modeling variables, leaving 581 patients for endpoint-specific MVI modeling.

Data collection

Demographic, clinical, laboratory, imaging, and pathological information was retrospectively retrieved from the electronic medical record system. The collected data covered baseline characteristics, liver function-related parameters, tumor-associated serum markers, nutritional and inflammatory indicators, preoperative conventional ultrasound findings, elastography measurements, and postoperative pathological results. Candidate variables for model development included age, sex, hepatitis history, alpha-fetoprotein (AFP), carcinoembryonic antigen (CEA), albumin, body mass index (BMI), prognostic nutritional index (PNI), Controlling Nutritional Status (CONUT) score, neutrophil-to-lymphocyte ratio (NLR), conventional ultrasound features, and shear wave elastography-derived parameters. Postoperative pathological findings, including microvascular invasion (MVI) status, were used as reference standards for endpoint determination.

Ultrasound and elastography assessment

Preoperative ultrasound assessment included conventional grayscale ultrasound, color Doppler flow imaging, and elastography. Conventional ultrasound variables included maximum tumor diameter, blood flow grade, tumor shape, and tumor margin. Shear wave elastography-derived quantitative parameters included the mean and maximum shear wave velocity values (Emean and Emax), recorded in meters per second (m/s).

All ultrasound examinations were completed before surgery by experienced sonographers according to a standardized acquisition protocol. Patients were examined after fasting and were positioned supine or in the left lateral decubitus position as needed. Conventional grayscale ultrasound was initially performed to identify the hepatic lesion and assess its location, maximal size, morphology, margin, internal echogenicity, and adjacent liver back-

ground. Color Doppler flow imaging was subsequently used to evaluate intratumoral and peritumoral vascularity. The maximum tumor diameter was recorded on the imaging plane showing the largest lesion dimension.

For elastography acquisition, the region of interest was positioned to include as much of the solid tumor component as possible while avoiding large vessels, bile ducts, calcified areas, obvious necrosis, and imaging artifacts. Images were obtained under stable respiratory conditions with minimal transducer compression to reduce measurement bias. When multiple frames were available, those with clear lesion margins, stable signal distribution or color filling, and without obvious motion or compression artifacts were selected for analysis. Only images meeting predefined quality criteria, including clear lesion margins, stable signal distribution, and absence of significant motion or compression artifacts, were included. Images not satisfying these criteria were excluded prior to radiomics analysis. Quantitative shear wave velocity parameters, including Emean and Emax, were recorded from the selected SWE images in m/s. All images were de-identified before analysis. Image quality was independently reviewed by experienced sonographers, and only images that satisfied the predefined quality criteria were included in the subsequent radiomics workflow. ROI delineation for radiomics analysis was initially performed manually on the de-identified grayscale ultrasound and elastography images by an experienced sonographer based on the lesion boundary identified on the image section showing the largest tumor area and was subsequently reviewed by a second experienced sonographer. Discrepancies between the two readers were resolved by consensus to ensure consistency of ROI delineation. Both readers were blinded to postoperative pathological results and endpoint classification during segmentation. Any disagreement was resolved by consensus before feature extraction.

Radiomics workflow

Radiomics analysis was performed using a standardized workflow that included image preprocessing, region-of-interest (ROI) segmentation, feature extraction, feature selection, and model construction. Prior to feature extraction, all images underwent resampling and gray-level normalization to reduce the influence of differences in image resolution and signal intensity. Feature normalization and dimensionality reduction procedures were applied to reduce the influence of variability and potential outliers in the dataset. Tumor ROIs were manually delineated on de-identified grayscale ultrasound and elastography images based on the lesion boundary identified on the image section showing the largest tumor area. The delineation process was performed without access to postoperative pathological results or endpoint classification. Only images with adequate quality and clear lesion margins were included in the radiomics analysis.

Radiomics features were extracted from both grayscale ultrasound and elastography images, including features derived from original images and wavelet-transformed images. The extracted features comprised first-order statistics, shape features, and texture features. Specifically, a total of 513 radiomics features were initially extracted from each lesion, including 162 histogram features and 351 texture features from the original and wavelet-transformed images. Detailed information on the feature extraction process is provided in Supplementary Table 1. The radiomics feature extraction package used in this study is publicly available at GitHub (github.com/mvallieres/radiomics).

Feature selection was performed in multiple steps. First, extracted features were standardized before downstream analysis. Second, univariable screening was applied to identify candidate features associated with the study endpoints. Third, redundant features were removed during the dimensionality-reduction process to reduce collinearity and overfitting. Finally, a sparse representation-based feature selection method was used to further reduce dimensionality and retain the most informative features, resulting in 10 radiomics features for each endpoint. Based on the selected radiomics features, a multilayer perceptron (MLP) classifier was constructed for prediction of 1-year recurrence and classification of MVI. The MLP architecture and training parameters were as follows: the network consisted of two hidden layers with 20 and 10 neurons, respectively, both using ReLU activation functions. The dropout ratio was set to 0.2. The

model was optimized using the Adam optimizer with a learning rate of 0.0005. Training was performed for 100 epochs with a batch size of 10. Feature selection and model training were performed in the training set, and model performance was subsequently evaluated in the validation set (Supplementary Figure 1).

Study endpoints

Two endpoints were defined in this study. The first endpoint was recurrence within 1 year after curative hepatectomy, determined on the basis of postoperative follow-up. The second endpoint was MVI, confirmed by postoperative pathological examination. Each endpoint was analyzed separately, and the same clinical, imaging, and radiomics modeling strategy was applied to both analyses.

Model construction and evaluation

For each study endpoint, three types of models were developed: a clinical model, a radiomics model, and a combined clinical-radiomics model. The entire dataset was allocated into a training cohort and an independent validation cohort at a ratio of 4:1 using random allocation with verification of baseline comparability; repeated random splitting was performed to minimize potential imbalance between cohorts. Feature selection and model hyperparameter optimization were performed exclusively within the training cohort to avoid information leakage and to ensure an unbiased evaluation of model performance. The final optimized models were subsequently assessed in the independent validation cohort. Given that the study was designed as a prediction-modeling analysis rather than a comparative study between balanced clinical groups, cohort matching procedures such as propensity score matching were not applied.

Model performance in the present study was primarily evaluated in terms of discrimination and classification ability using the area under the receiver operating characteristic curve (AUC), accuracy (ACC), sensitivity (SEN), specificity (SPE), positive predictive value (PPV), and negative predictive value (NPV). The present study was designed as an exploratory prediction modeling analysis, and the evaluation focused primarily on discrimination performance rather than clinical decision-making utility. Because this was a retrospective exploratory modeling study aimed at initial model development and internal validation, formal evaluation of calibration and clinical net benefit, such as calibration curve analysis and decision curve analysis (DCA), was not included in the current workflow.

Statistical analysis

Clinical and imaging variables were first screened by univariable analysis. Because several nutrition-related variables were mathematically related, including composite indicators partly derived from serum albumin and lymphocyte-related parameters, collinearity among nutrition-related candidate predictors was considered before final model construction. Strongly overlapping nutritional variables were interpreted with caution, and representative composite indices were preferentially emphasized to improve biological interpretability and model stability. Continuous variables were compared using the independent-samples t test or Mann-Whitney U test, as appropriate, and categorical variables were compared using the chi-square test or Fisher's exact test. The corresponding test statistics are reported in the Supplementary Tables 2 and 3 for baseline comparisons between the training and validation cohorts. Variables showing statistical significance in univariable analysis were subsequently entered into least absolute shrinkage and selection operator (LASSO) regression for further dimensionality reduction and selection of the final feature subset for model construction. Statistical significance was defined according to the prespecified thresholds used in the original study workflow, and a two-sided $P<0.05$ was considered statistically significant. Because the study was designed as a prediction modeling analysis rather than a comparative study between balanced exposure groups, strict baseline equivalence between the training and validation cohorts was not a methodological requirement. Minor imbalances were considered acceptable and unlikely to introduce systematic bias in model performance.

Results

Baseline characteristics

A total of 619 patients with HCC were included in the recurrence analysis. For the MVI

Table 1. Baseline characteristics of patients in the training and validation cohorts for 1-year recurrence analysis

Variable	All (N = 619)	Validation cohort (n = 124)	Training cohort (n = 495)	*P* value
Sex				0.710
Male	477 (77.1%)	94 (75.8%)	383 (77.4%)	
Female	142 (22.9%)	30 (24.2%)	112 (22.6%)	
Ethnicity				0.717
Han	601 (97.1%)	121 (97.6%)	480 (97.0%)	
Non-Han	18 (2.9%)	3 (2.4%)	15 (3.0%)	
Age, years	56.05±10.66	56.66±10.57	53.80±10.70	0.006
Body mass index, kg/m^2	24.03±3.22	24.00±3.20	24.12±3.32	0.705
Subjective Global Assessment (SGA)				0.434
Well nourished	592 (95.6%)	117 (94.4%)	475 (96.0%)	
Mild-to-moderate malnutrition	27 (4.4%)	7 (5.6%)	20 (4.0%)	
Mini Nutritional Assessment (MNA)				0.183
≥24	550 (88.9%)	106 (85.5%)	444 (89.7%)	
17-23.5	69 (11.1%)	18 (14.5%)	51 (10.3%)	
History of tumor				0.934
No	585 (94.5%)	117 (94.4%)	468 (94.5%)	
Yes	34 (5.5%)	7 (5.6%)	27 (5.5%)	
History of hepatitis				0.012
No	272 (43.9%)	42 (33.9%)	230 (46.5%)	
Yes	347 (56.1%)	82 (66.1%)	265 (53.5%)	
Antiviral therapy				0.061
No	418 (67.5%)	75 (60.5%)	343 (69.3%)	
Yes	201 (32.5%)	49 (39.5%)	152 (30.7%)	
Number of tumors				0.968
Solitary	495 (80.0%)	99 (79.8%)	396 (80.0%)	
Multiple	124 (20.0%)	25 (20.2%)	99 (20.0%)	
Surgical approach				0.034
Laparoscopic	591 (95.5%)	114 (91.9%)	477 (96.4%)	
Open	28 (4.5%)	10 (8.1%)	18 (3.6%)	
Maximum tumor diameter, mm	44.50 [28.40, 67.50]	47.40 [28.45, 69.28]	44.30 [28.40, 66.70]	0.489
Peritumoral cirrhosis				0.001
No	227 (36.7%)	30 (24.2%)	197 (39.8%)	
Yes	392 (63.3%)	94 (75.8%)	298 (60.2%)	
Histopathological subtype				0.777
Thick trabecular type	255 (41.2%)	51 (41.1%)	204 (41.2%)	
Thin trabecular type	65 (10.5%)	12 (9.7%)	53 (10.7%)	
Acinar type	83 (13.4%)	17 (13.7%)	66 (13.3%)	
Solid-sheet type	27 (4.4%)	3 (2.4%)	24 (4.8%)	
Other types	189 (30.5%)	41 (33.1%)	148 (29.9%)	
Tumor differentiation				0.325
Poor	289 (46.7%)	53 (42.7%)	236 (47.7%)	
Moderate/Well	330 (53.3%)	71 (57.3%)	259 (52.3%)	
Hep-1expression				0.984
No	314 (50.7%)	63 (50.8%)	251 (50.7%)	
Yes	305 (49.3%)	61 (49.2%)	244 (49.3%)	
Arginase expression				0.792
No	288 (46.5%)	59 (47.6%)	229 (46.3%)	
Yes	331 (53.5%)	65 (52.4%)	266 (53.7%)	

GPC-3 expression				0.793
No	326 (52.7%)	64 (51.6%)	262 (52.9%)	
Yes	293 (47.3%)	60 (48.4%)	233 (47.1%)	
CD34 expression				0.469
No	242 (39.1%)	52 (41.9%)	190 (38.4%)	
Yes	377 (60.9%)	72 (58.1%)	305 (61.6%)	
Tumor shape				0.132
Round	327 (52.8%)	73 (58.9%)	254 (51.3%)	
Irregular	292 (47.2%)	51 (41.1%)	241 (48.7%)	
Echogenicity				0.396
Hypoechoic	435 (70.3%)	91 (73.4%)	344 (69.5%)	
Hyperechoic	184 (29.7%)	33 (26.6%)	151 (30.5%)	
Tumor margin				0.324
Smooth	335 (54.1%)	72 (58.1%)	263 (53.1%)	
Irregular	284 (45.9%)	52 (41.9%)	232 (46.9%)	
Blood flow signal				0.101
Absent	211 (34.1%)	50 (40.3%)	161 (32.5%)	
Present	408 (65.9%)	74 (59.7%)	334 (67.5%)	
Peritumoral Emax, m/s	1.47 [1.24, 1.85]	1.48 [1.25, 1.86]	1.47 [1.24, 1.84]	0.688
Peritumoral Emean, m/s	1.40 [1.17, 1.75]	1.41 [1.19, 1.77]	1.39 [1.17, 1.75]	0.797
Intratumoral Emax, m/s	2.26 [1.87, 2.75]	2.29 [1.87, 2.76]	2.25 [1.87, 2.74]	0.992
Intratumoral Emean, m/s	1.78 [1.48, 2.16]	1.74 [1.48, 2.13]	1.78 [1.48, 2.17]	0.703
Total protein, g/L	67.60 [64.10, 71.00]	67.60 [64.18, 70.78]	67.60 [64.10, 71.30]	0.883
Albumin, g/L	41.40 [39.20, 44.00]	41.20 [39.13, 43.50]	41.50 [39.20, 44.10]	0.390
Lymphocyte count, $\times 10^9$/L	2.00 [2.00, 2.00]	2.00 [2.00, 2.00]	2.00 [2.00, 2.00]	0.434
Prognostic Nutritional Index (PNI)	51.40 [49.20, 54.00]	51.20 [49.13, 53.50]	51.50 [49.20, 54.10]	0.383
Controlling Nutritional Status (CONUT) score				0.613
0-1	583 (94.2%)	117 (94.4%)	466 (94.1%)	
2-4	9 (1.5%)	2 (1.6%)	7 (1.4%)	
5-8	9 (1.5%)	2 (1.6%)	7 (1.4%)	
9-10	10 (1.6%)	3 (2.4%)	7 (1.4%)	
11-12	8 (1.3%)	0 (0.0%)	8 (1.6%)	
ALT, U/L	26.00 [17.00, 39.00]	27.00 [15.00, 41.75]	26.00 [17.00, 39.00]	0.808
AST, U/L	26.00 [19.00, 37.00]	25.50 [19.00, 36.00]	26.00 [19.00, 37.00]	0.921
GGT, U/L	52.00 [28.00, 82.00]	50.00 [26.25, 81.50]	53.00 [29.00, 82.00]	0.758
INR	1.00 [0.95, 1.04]	1.00 [0.94, 1.04]	1.00 [0.95, 1.04]	0.993
PT, s	12.00 [11.40, 12.40]	12.00 [11.33, 12.50]	12.00 [11.40, 12.40]	0.917
PLT, $\times 10^9$/L	161.00 [117.00, 214.00]	160.50 [110.00, 213.00]	162.00 [119.00, 215.00]	0.52
Neutrophil count, $\times 10^9$/L	3.79 [2.90, 3.79]	3.65 [3.03, 3.79]	3.79 [2.87, 3.79]	0.587
NLR, $\times 10^9$/L	1.90 [1.48, 1.97]	1.90 [1.52, 1.93]	1.90 [1.45, 1.97]	0.882
Glucose, mmol/L	5.17 [4.72, 5.17]	5.17 [4.73, 5.19]	5.17 [4.70, 5.17]	0.518
AFP, ng/mL	19.90 [3.10, 811.00]	14.25 [3.00, 572.25]	19.90 [3.10, 971.00]	0.504
CEA, ng/mL	2.30 [1.40, 3.50]	2.25 [1.40, 3.60]	2.30 [1.30, 3.50]	0.704

Note: SGA, Subjective Global Assessment; MNA, Mini Nutritional Assessment; PNI, Prognostic Nutritional Index; CONUT, Controlling Nutritional Status; ALT, alanine aminotransferase; AST, aspartate aminotransferase; GGT, gamma-glutamyl transferase; INR, international normalized ratio; PT, prothrombin time; NLR, neutrophil-to-lymphocyte ratio; AFP, alpha-fetoprotein; CEA, carcinoembryonic antigen; MVI, microvascular invasion. Data are presented as mean ± standard deviation, median (interquartile range), or n (%), as appropriate. *P* values indicate comparisons between the training and validation cohorts. The corresponding statistical tests and test statistics are provided in Supplementary Table 2.

analysis, 581 of these 619 patients were retained as an endpoint-specific cohort after exclusion of 38 patients without complete postoperative pathological MVI assessment and/or key modeling variables. Baseline characteristics of the training and validation cohorts for the recurrence and MVI analyses are presented in **Tables 1** and **2**, respectively. Although

Table 2. Baseline characteristics of patients in the training and validation cohorts for microvascular invasion analysis

Variable	All (N = 581)	Validation cohort (n = 116)	Training cohort (n = 465)	*P* value
Sex				0.480
Male	450 (77.5%)	87 (75.0%)	363 (78.1%)	
Female	131 (22.5%)	29 (25.0%)	102 (21.9%)	
Ethnicity				0.031
Han	564 (97.1%)	116 (100.0%)	448 (96.3%)	
Non-Han	17 (2.9%)	0 (0.0%)	17 (3.7%)	
Age, years	56.08±10.56	56.31±10.05	56.02±10.70	0.789
Body mass index, kg/m^2	23.99±3.21	23.91±3.09	24.01±3.24	0.771
Subjective Global Assessment (SGA)				0.056
Well nourished	555 (95.5%)	107 (92.2%)	448 (96.3%)	
Mild-to-moderate malnutrition	26 (4.5%)	9 (7.8%)	17 (3.7%)	
Mini Nutritional Assessment (MNA)				0.941
≥24	517 (89.0%)	103 (88.8%)	414 (89.0%)	
17-23.5	64 (11.0%)	13 (11.2%)	51 (11.0%)	
History of tumor				0.550
No	555 (95.5%)	112 (96.6%)	443 (95.3%)	
Yes	26 (4.5%)	4 (3.4%)	22 (4.7%)	
History of hepatitis				0.545
No	246 (42.3%)	52 (44.8%)	194 (41.7%)	
Yes	335 (57.7%)	64 (55.2%)	271 (58.3%)	
Antiviral therapy				0.770
No	384 (66.1%)	78 (67.2%)	306 (65.8%)	
Yes	197 (33.9%)	38 (32.8%)	159 (34.2%)	
Number of tumors				0.448
Solitary	461 (79.3%)	95 (81.9%)	366 (78.7%)	
Multiple	120 (20.7%)	21 (18.1%)	99 (21.3%)	
Surgical approach				0.775
Laparoscopic	553 (95.2%)	111 (95.7%)	442 (95.1%)	
Open	28 (4.8%)	5 (4.3%)	23 (4.9%)	
Maximum tumor diameter, mm	44.40 [28.55, 67.35]	43.20 [27.63, 69.53]	45.00 [28.65, 66.70]	0.729
Peritumoral cirrhosis				0.010
No	206 (35.5%)	53 (45.7%)	153 (32.9%)	
Yes	375 (64.5%)	63 (54.3%)	312 (67.1%)	
Histopathological subtype				0.195
Thick trabecular type	255 (43.9%)	53 (45.7%)	202 (43.4%)	
Thin trabecular type	60 (10.3%)	12 (10.3%)	48 (10.3%)	
Acinar type	57 (9.8%)	17 (14.7%)	40 (8.6%)	
Solid-sheet type	27 (4.6%)	6 (5.2%)	21 (4.5%)	
Other types	182 (31.3%)	28 (24.1%)	154 (33.1%)	
Tumor differentiation				0.040
Poor	280 (48.2%)	46 (39.7%)	234 (50.3%)	
Moderate/Well	301 (51.8%)	70 (60.3%)	231 (49.7%)	
Hep-1 expression				0.191
No	282 (48.5%)	50 (43.1%)	232 (49.9%)	
Yes	299 (51.5%)	66 (56.9%)	233 (50.1%)	
Arginase expression				0.249
No	253 (43.5%)	45 (38.8%)	208 (44.7%)	
Yes	328 (56.5%)	71 (61.2%)	257 (55.3%)	

GPC-3 expression				0.395
No	291 (50.1%)	54 (46.6%)	237 (51.0%)	
Yes	290 (49.9%)	62 (53.4%)	228 (49.0%)	
CD34 expression				0.173
No	212 (36.5%)	36 (31.0%)	176 (37.8%)	
Yes	369 (63.5%)	80 (69.0%)	289 (62.2%)	
Tumor shape				0.077
Round	313 (53.9%)	71 (61.2%)	242 (52.0%)	
Irregular	268 (46.1%)	45 (38.8%)	223 (48.0%)	
Echogenicity				0.264
Hypoechoic	406 (69.9%)	86 (74.1%)	320 (68.8%)	
Hyperechoic	175 (30.1%)	30 (25.9%)	145 (31.2%)	
Tumor margin				0.269
Smooth	314 (54.0%)	68 (58.6%)	246 (52.9%)	
Irregular	267 (46.0%)	48 (41.4%)	219 (47.1%)	
Blood flow signal				0.748
Absent	198 (34.1%)	41 (35.3%)	157 (33.8%)	
Present	383 (65.9%)	75 (64.7%)	308 (66.2%)	
Peritumoral Emax, m/s	1.47 [1.24, 1.87]	1.44 [1.24, 1.90]	1.48 [1.24, 1.85]	0.541
Peritumoral Emean, m/s	1.41 [1.18, 1.77]	1.39 [1.19, 1.79]	1.41 [1.17, 1.77]	0.591
Intratumoral Emax, m/s	2.26 [1.91, 2.76]	2.26 [1.88, 2.75]	2.26 [1.91, 2.76]	0.921
Intratumoral Emean, m/s	1.78 [1.50, 2.17]	1.77 [1.47, 2.19]	1.79 [1.51, 2.17]	0.987
Total protein, g/L	67.60 [64.10, 71.00]	67.80 [65.30, 71.18]	67.50 [63.90, 70.95]	0.245
Albumin, g/L	41.30 [39.10, 43.95]	41.65 [39.63, 44.38]	41.30 [39.00, 43.90]	0.323
Lymphocyte count, $\times 10^9$/L	2.00 [2.00, 2.00]	2.00 [2.00, 2.00]	2.00 [2.00, 2.00]	0.775
Prognostic Nutritional Index (PNI)	51.30 [49.10, 53.95]	51.65 [49.63, 54.38]	51.30 [49.00, 53.90]	0.346
Controlling Nutritional Status (CONUT) score				0.773
0-1	546 (94.0%)	109 (94.0%)	437 (94.0%)	
2-4	9 (1.5%)	3 (2.6%)	6 (1.3%)	
5-8	9 (1.5%)	2 (1.7%)	7 (1.5%)	
9-10	10 (1.7%)	1 (0.9%)	9 (1.9%)	
11-12	7 (1.2%)	1 (0.9%)	6 (1.3%)	
ALT, U/L	27.00 [17.00, 40.00]	26.00 [17.00, 38.75]	27.00 [17.00, 41.00]	0.229
AST, U/L	26.00 [19.00, 37.00]	24.00 [19.00, 35.75]	27.00 [19.00, 37.50]	0.24
GGT, U/L	53.00 [29.00, 82.00]	50.00 [29.00, 79.50]	54.00 [29.00, 82.50]	0.747
INR	1.00 [0.95, 1.04]	1.00 [0.93, 1.04]	1.00 [0.95, 1.04]	0.179
PT, s	12.00 [11.40, 12.40]	11.95 [11.23, 12.40]	12.00 [11.40, 12.50]	0.208
PLT, $\times 10^9$/L	160.00 [116.00, 212.50]	170.50 [128.25, 225.75]	157.00 [114.00, 209.00]	0.028
Neutrophil count, $\times 10^9$/L	3.79 [2.90, 3.79]	3.79 [2.88, 3.79]	3.77 [2.90, 3.79]	0.72
NLR, $\times 10^9$/L	1.90 [1.47, 1.97]	1.90 [1.46, 1.98]	1.90 [1.47, 1.97]	0.645
Glucose, mmol/L	5.17 [4.73, 5.17]	5.17 [4.74, 5.17]	5.17 [4.73, 5.17]	0.205
AFP, ng/mL	17.90 [3.10, 774.50]	22.60 [3.13, 912.75]	16.50 [3.10, 774.50]	0.804
CEA, ng/mL	2.30 [1.40, 3.50]	2.00 [1.20, 2.80]	2.30 [1.40, 3.60]	0.012

Note: SGA, Subjective Global Assessment; MNA, Mini Nutritional Assessment; PNI, Prognostic Nutritional Index; CONUT, Controlling Nutritional Status; ALT, alanine aminotransferase; AST, aspartate aminotransferase; GGT, gamma-glutamyl transferase; INR, international normalized ratio; PT, prothrombin time; NLR, neutrophil-to-lymphocyte ratio; AFP, alpha-fetoprotein; CEA, carcinoembryonic antigen; MVI, microvascular invasion. Data are presented as mean ± standard deviation, median (interquartile range), or n (%), as appropriate. *P* values indicate comparisons between the training and validation cohorts. The corresponding statistical tests and test statistics are provided in Supplementary Table 3. The MVI cohort was an endpoint-specific subset of the overall 619-patient cohort; 38 patients were excluded from the MVI analysis because of incomplete postoperative pathological MVI assessment and/or missing key modeling variables.

minor differences in several baseline variables were observed between the training and validation cohorts in both the recurrence and MVI analyses, these differences were considered acceptable in the context of prediction modeling and were not expected to introduce system-

Table 3. Comparison of the predictive performance of individual clinical indicators and radiomics features for 1-year postoperative recurrence in hepatocellular carcinoma

Clinical features	AUC	ACC	SEN	SPE	PPV	NPV
Maximum tumor diameter	0.599	0.511	0.712	0.456	0.262	0.854
Tumor margin	0.578	0.649	0.432	0.708	0.286	0.821
Intratumoral Emax	0.576	0.565	0.545	0.571	0.256	0.822
Intratumoral Emean	0.573	0.611	0.492	0.643	0.272	0.824
Radiomics features						
WT6IHM	0.581	0.430	0.811	0.326	0.246	0.864
WT7IRMS	0.575	0.357	0.932	0.201	0.240	0.916
WT7IHS	0.576	0.564	0.568	0.563	0.260	0.828
WT3IRMS	0.576	0.354	0.932	0.197	0.239	0.914
WT3IHS	0.575	0.533	0.614	0.511	0.254	0.830
WT6TGLSZMHGZE	0.581	0.590	0.530	0.606	0.267	0.826
IHK	0.559	0.591	0.508	0.614	0.263	0.821
WT5IK	0.575	0.622	0.485	0.659	0.278	0.825
WT4TGLRLMGLV	0.576	0.481	0.765	0.405	0.258	0.864
WT1ISD	0.571	0.368	0.879	0.230	0.236	0.875

Note: AUC, area under the receiver operating characteristic curve; ACC, accuracy; SEN, sensitivity; SPE, specificity; PPV, positive predictive value; NPV, negative predictive value.

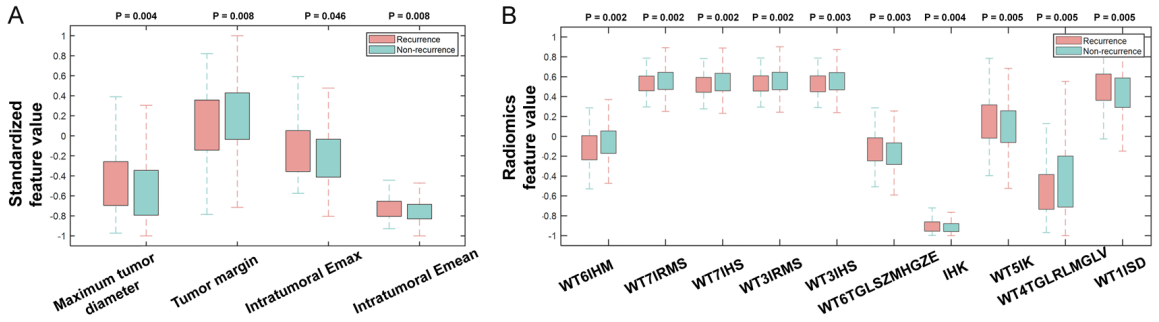

Figure 2. Comparison of clinical and radiomics features between recurrence and non-recurrence groups. A. Boxplots showing differences in representative clinical and imaging variables between the recurrence and non-recurrence groups, including maximum tumor diameter, tumor margin, intratumoral Emax, and intratumoral Emean. The x-axis indicates recurrence status, and the y-axis of each panel indicates the corresponding variable with units where applicable. Exact *P* values are shown in the figure. B. Paired boxplots showing the distribution of 10 selected radiomics features associated with 1-year postoperative recurrence, including 7 intensity features and 3 texture features derived from grayscale ultrasound and elastography images or their wavelet-transformed images.

atic bias in model performance. Univariable comparisons between recurrence and non-recurrence groups and between MVI-positive and MVI-negative groups are provided in Supplementary Tables 2 and 3, respectively.

Prediction of 1-year recurrence

Clinical candidate variables: For prediction of 1-year recurrence, univariable analysis identified Subjective Global Assessment (SGA), tumor blood flow, tumor shape, maximum tumor diameter, Controlling Nutritional Status (CONUT) score, age, tumor margin, mean shear wave velocity (Emean) and maximum shear wave velocity (Emax) were identified as significant candidate variables (**Table 3**). Paired boxplot analysis showed differences between the recurrence and non-recurrence groups in several representative variables, including maximum tumor diameter, tumor margin, Emean, and Emax (**Figure 2A**). Because CONUT is a composite nutritional index, its component variables were not interpreted as separate

Table 4. Comparison of the classification performance of different models for predicting 1-year postoperative recurrence

Dataset	Model	AUC	ACC	SEN	SPE	PPV	NPV
Cross-validation set (VA)	Clinical	0.567	0.580	0.513	0.601	0.289	0.796
Cross-validation set (VA)	Radiomics	0.660	0.743	0.412	0.848	0.462	0.820
Cross-validation set (VA)	Clinical + radiomics	0.675	0.786	0.193	0.973	0.697	0.792
Independent test set (TE)	Clinical	0.656	0.661	0.455	0.706	0.250	0.857
Independent test set (TE)	Radiomics	0.759	0.766	0.364	0.853	0.348	0.861
Independent test set (TE)	Clinical + radiomics	0.771	0.774	0.545	0.824	0.400	0.894

Note: AUC, area under the receiver operating characteristic curve; ACC, accuracy; SEN, sensitivity; SPE, specificity; PPV, positive predictive value; NPV, negative predictive value; VA, cross-validation set; TE, independent test set.

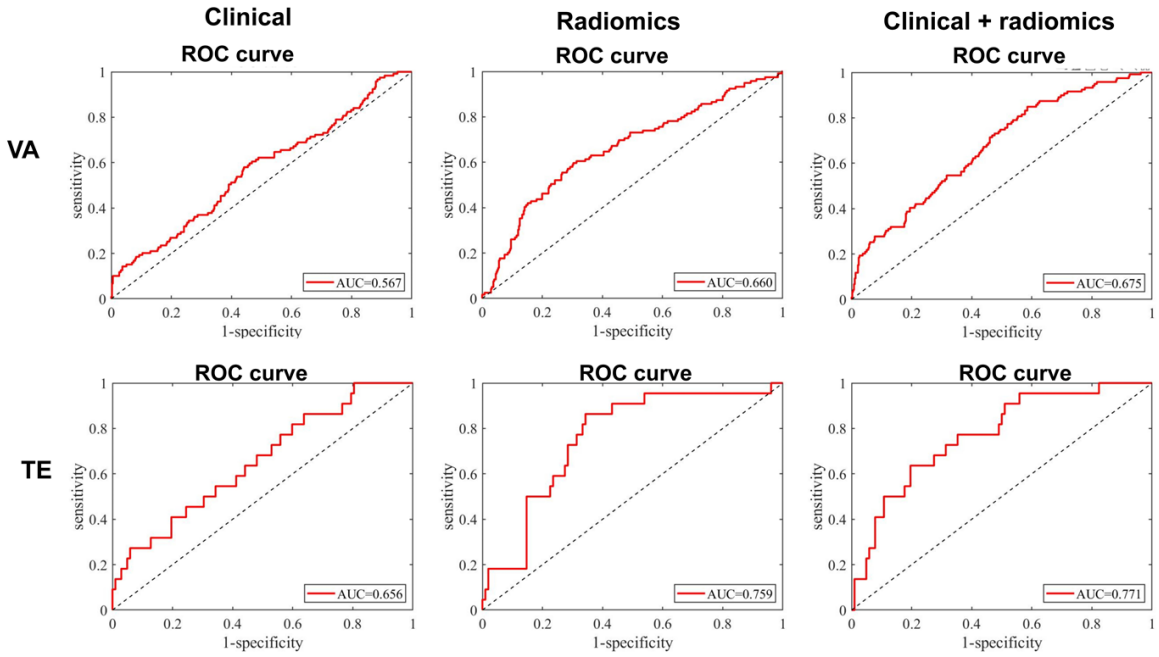

Figure 3. Receiver operating characteristic (ROC) curves of different models for predicting 1-year postoperative recurrence. The upper panel shows the ROC curves of the clinical model, radiomics model, and combined clinical-radiomics model in the cross-validation set (VA), and the lower panel shows the corresponding ROC curves in the independent test set (TE). The AUCs of the three models were 0.567, 0.660, and 0.675 in the cross-validation set, and 0.656, 0.759, and 0.771 in the independent test set, respectively.

independent biological signals in the recurrence analysis.

Radiomics features: Ten radiomics features associated with 1-year recurrence were retained, including 7 intensity features and 3 texture features extracted from grayscale ultrasound and elastography images, either from the original images or from wavelet-transformed images (**Table 3**; **Figure 2B**). These selected features represented differences in gray-level distribution, texture pattern, and spatial heterogeneity between the two groups.

Model performance: For prediction of 1-year recurrence, the combined clinical-radiomics model achieved the best overall performance among the three models. In the cross-validation set, the area under the receiver operating characteristic curve (AUC) values of the clinical, radiomics, and combined models were 0.567, 0.660, and 0.675, respectively. In the independent test set, the corresponding AUC values were 0.656, 0.759, and 0.771, respectively (**Table 4**; **Figure 3**). These results showed that the combined model provided the highest discriminative ability in both datasets, whereas

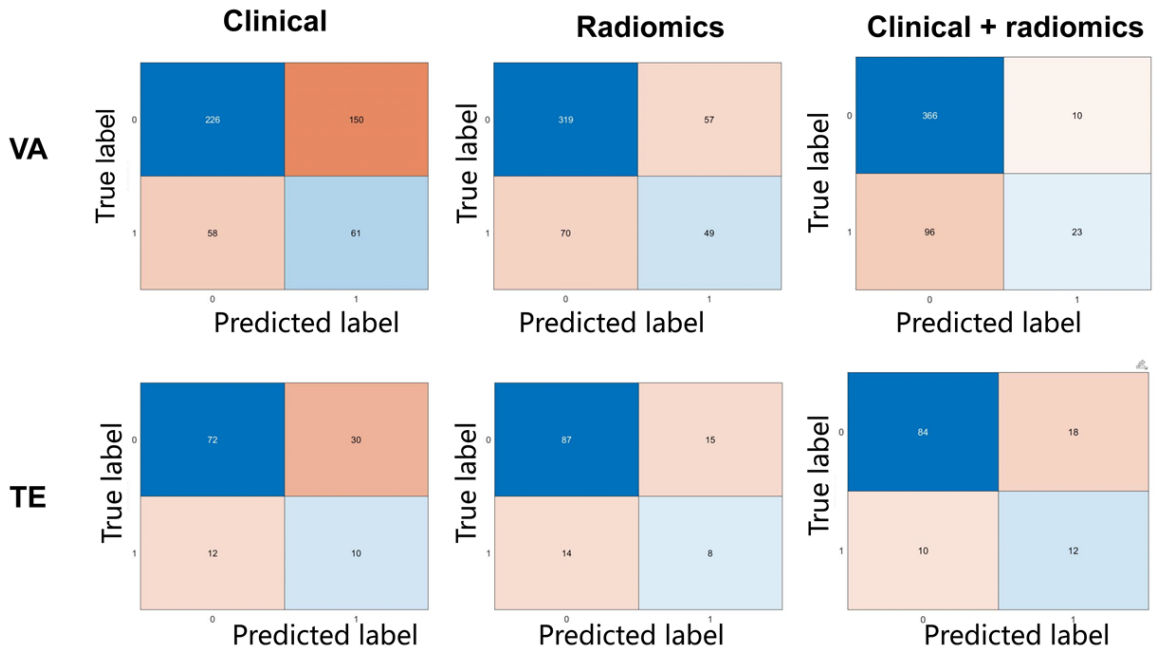

Figure 4. Confusion matrices of different models for predicting 1-year postoperative recurrence. The upper panel shows the confusion matrices of the clinical model, radiomics model, and combined clinical-radiomics model in the cross-validation set (VA), and the lower panel shows the corresponding confusion matrices in the independent test set (TE). The horizontal axis represents the predicted class, and the vertical axis represents the true class. The results showed that the combined model had the strongest ability to identify non-recurrent patients in the cross-validation set and demonstrated superior overall classification performance in the independent test set.

the radiomics model alone also outperformed the clinical model, particularly in the independent test set.

Confusion matrix analysis further demonstrated differences in classification performance among the three models (**Figure 4**). In the cross-validation set, the combined model showed improved identification of non-recurrent cases compared with the clinical model and the radiomics model. In the independent test set, the combined model demonstrated the best overall classification performance.

The distribution plots of predictive scores showed that all three models had a certain degree of risk stratification ability in both the cross-validation and independent test sets (**Figure 5**). However, substantial overlap in predictive scores was observed between recurrent and non-recurrent cases in the clinical model, indicating limited discriminative performance. By comparison, the radiomics model showed improved separation between the two groups, whereas the combined model demonstrated the clearest stratification pattern, with recurrent cases more frequently distributed in the high-score range and non-recurrent cases more frequently distributed in the low-score range. A similar trend was observed in the independent test set, supporting the stability and generalizability of the combined model.

Prediction of MVI

Clinical candidate variables: For MVI prediction, univariable analysis identified prognostic nutritional index (PNI), albumin, total protein, neutrophil-to-lymphocyte ratio (NLR), prothrombin time (PT), and international normalized ratio (INR) as significant clinical candidate variables (**Figure 6A**). PNI and albumin showed relatively stronger statistical significance than the other variables. After LASSO regression, PNI, albumin, NLR, and total albumin were retained as the final clinical predictors for model development. Because some of these nutritional variables were mathematically related, they were interpreted as overlapping host-related nutritional-inflammatory signals rather than completely independent biological factors (**Table 5**).

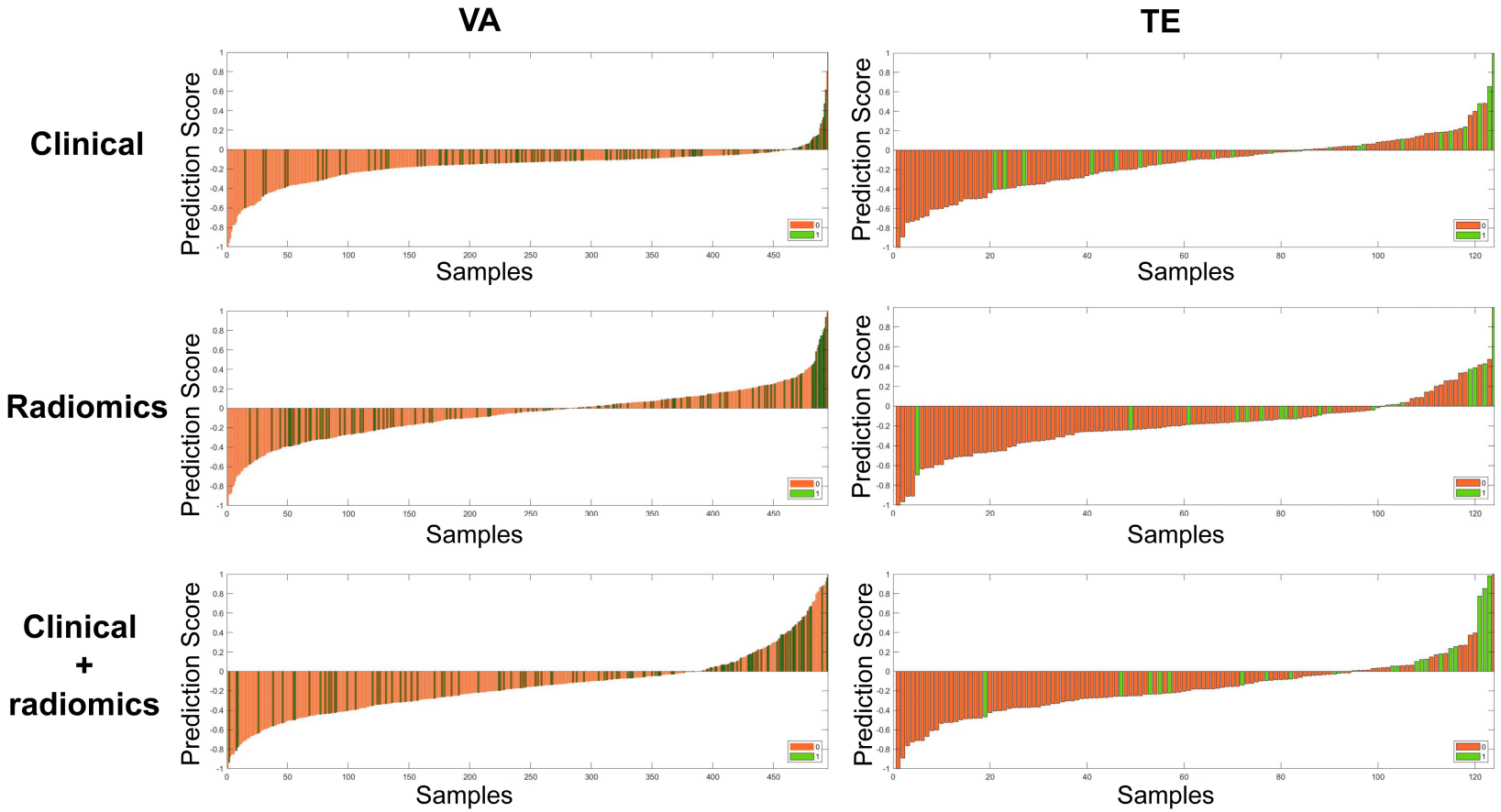

Figure 5. Distribution of predictive scores of different models for 1-year postoperative recurrence. The upper panel shows the predictive score distributions of the clinical model, radiomics model, and combined clinical-radiomics model in the cross-validation set (VA), and the lower panel shows the corresponding distributions in the independent test set (TE). The horizontal axis represents individual samples, and the vertical axis represents predictive scores. Compared with the clinical model, the radiomics model and the combined model showed clearer separation between recurrent and non-recurrent cases, with the combined model demonstrating the most distinct stratification pattern.

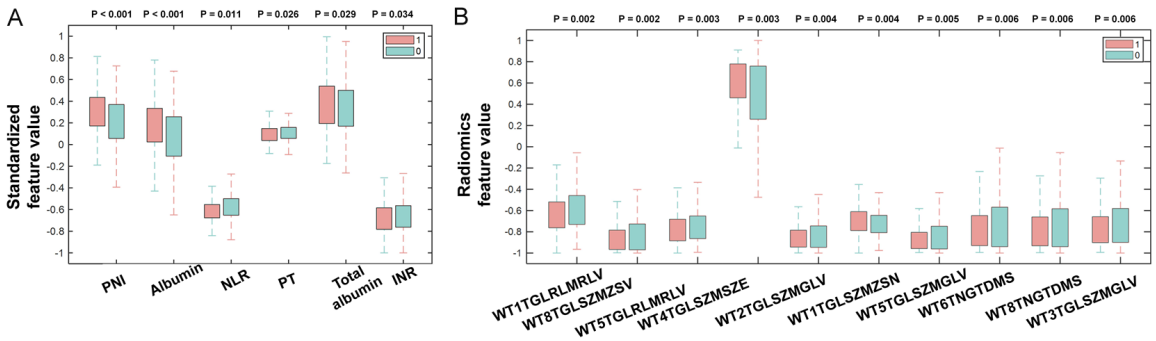

Figure 6. Comparison of clinical and radiomics features between MVI-positive and MVI-negative groups. A. Boxplots showing the distributions of PNI, albumin, NLR, PT, total protein, and INR in the MVI-positive and MVI-negative groups. The x-axis indicates MVI status, and the y-axis of each panel indicates the corresponding variable with units where applicable. Exact *P* values are shown in the figure. B. Paired boxplots showing the distributions of selected radiomics features associated with MVI.

Table 5. Comparison of the predictive performance of individual clinical indicators and radiomics features for MVI in hepatocellular carcinoma

Clinical features	AUC	ACC	SEN	SPE	PPV	NPV
PNI	0.610	0.590	0.532	0.645	0.586	0.594
Albumin	0.610	0.590	0.532	0.645	0.586	0.594
NLR	0.560	0.549	0.869	0.247	0.521	0.667
Total Albumin	0.547	0.546	0.472	0.615	0.536	0.553
Radiomics features						
WT1TGLRLMRLV	0.578	0.573	0.433	0.706	0.581	0.569
WT8TGLSZMZSV	0.531	0.540	0.706	0.385	0.520	0.581
WT5TGLRLMRLV	0.568	0.583	0.504	0.659	0.582	0.585
WT4TGLSZMSZE	0.553	0.554	0.787	0.334	0.527	0.625
WT2TGLSZMGLV	0.542	0.547	0.720	0.385	0.525	0.593
WT1TGLSZMZSN	0.553	0.554	0.344	0.753	0.567	0.549
WT5TGLSZMGLV	0.530	0.542	0.741	0.355	0.520	0.592
WT6TNGTDMS	0.533	0.535	0.706	0.375	0.516	0.574
WT8TNGTDMS	0.534	0.542	0.688	0.405	0.522	0.579
WT3TGLSZMGLV	0.543	0.552	0.592	0.515	0.535	0.572

Note: AUC, area under the receiver operating characteristic curve; ACC, accuracy; SEN, sensitivity; SPE, specificity; PPV, positive predictive value; NPV, negative predictive value; PNI, Prognostic Nutritional Index; NLR, Neutrophil-to-lymphocyte ratio.

Radiomics features: During univariable screening, 18 radiomics features significantly associated with MVI were identified, all of which were texture features. These features were mainly derived from wavelet-transformed grayscale ultrasound and elastography images and included parameters from the gray-level run length matrix (GLRLM), gray-level size zone matrix (GLSZM), and neighborhood gray-tone difference matrix (NGTDM) (**Figure 6B**). After LASSO regression, 10 radiomics features were retained for subsequent model construction, including WT1TGLRLMRLV, WT8TGLSZMZSV, WT5TGLRLMRLV, WT4TGLSZMSZE, WT2TGLSZMGLV, WT1TGLSZMZSN, WT5TGLSZMGLV, WT6TNGTDMS, WT8TNGTDMS, and WT3TGLSZMGLV (**Table 5**).

Model performance: For MVI prediction, the combined clinical-radiomics model achieved the highest performance among the three models. In the cross-validation set, the AUCs of the clinical, radiomics, and combined models were 0.836, 0.667, and 0.860, respectively. In the independent test set, the corresponding AUCs were 0.793, 0.661, and 0.819, respectively (**Table 6**; **Figure 7**). The radiomics model alone performed worse than the clini-

Table 6. Comparison of the classification performance of different models for predicting MVI in hepatocellular carcinoma

Dataset	Model	AUC	ACC	SEN	SPE	PPV	NPV
Cross-validation set (VA)	Clinical	0.836	0.768	0.800	0.737	0.741	0.797
Cross-validation set (VA)	Radiomics	0.667	0.655	0.689	0.622	0.637	0.675
Cross-validation set (VA)	Clinical + radiomics	0.860	0.796	0.782	0.808	0.793	0.798
Independent test set (TE)	Clinical	0.793	0.733	0.941	0.604	0.716	0.762
Independent test set (TE)	Radiomics	0.661	0.621	0.730	0.491	0.630	0.605
Independent test set (TE)	Clinical + radiomics	0.819	0.776	0.810	0.736	0.785	0.765

Note: AUC, area under the receiver operating characteristic curve; ACC, accuracy; SEN, sensitivity; SPE, specificity; PPV, positive predictive value; NPV, negative predictive value; VA, cross-validation set; TE, independent test set.

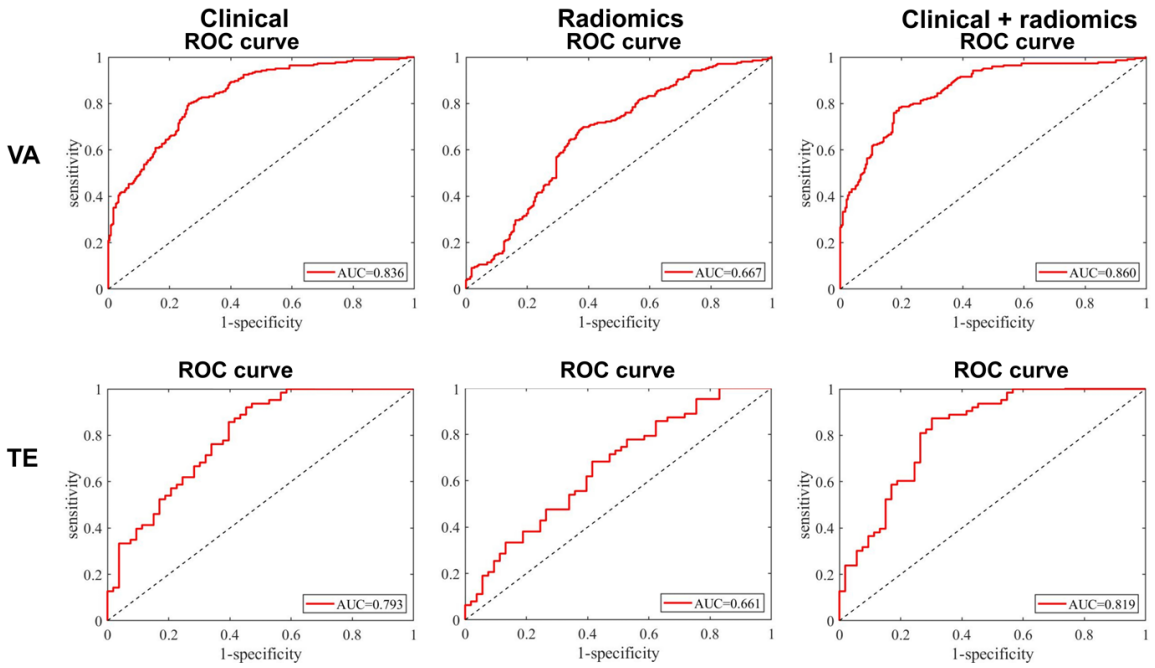

Figure 7. Receiver operating characteristic (ROC) curves of different models for predicting microvascular invasion (MVI). The upper panel shows the ROC curves of the clinical model, radiomics model, and combined clinical-radiomics model in the cross-validation set (VA), and the lower panel shows the corresponding ROC curves in the independent test set (TE). The AUCs of the three models were 0.836, 0.667, and 0.860 in the cross-validation set, and 0.793, 0.661, and 0.819 in the independent test set, respectively.

cal model, whereas the combined model consistently showed the highest discriminative ability.

Confusion matrices showed that the combined model had better overall classification performance than the radiomics model and achieved a more balanced classification pattern in the independent test set (**Figure 8**). Consistently, predictive score distribution plots demonstrated clearer separation between MVI-positive and MVI-negative cases in the combined model than in the radiomics model, with the clinical model also showing relatively good stratification ability (**Figure 9**).

Discussion

In this study, we developed a preoperative multimodal prediction framework for two clinically important endpoints in HCC, namely recurrence within 1 year after curative hepatectomy and pathological MVI. By integrating routine conventional ultrasound, elastography, and clinical nutritional indicators, we found that the combined clinical-radiomics models achieved

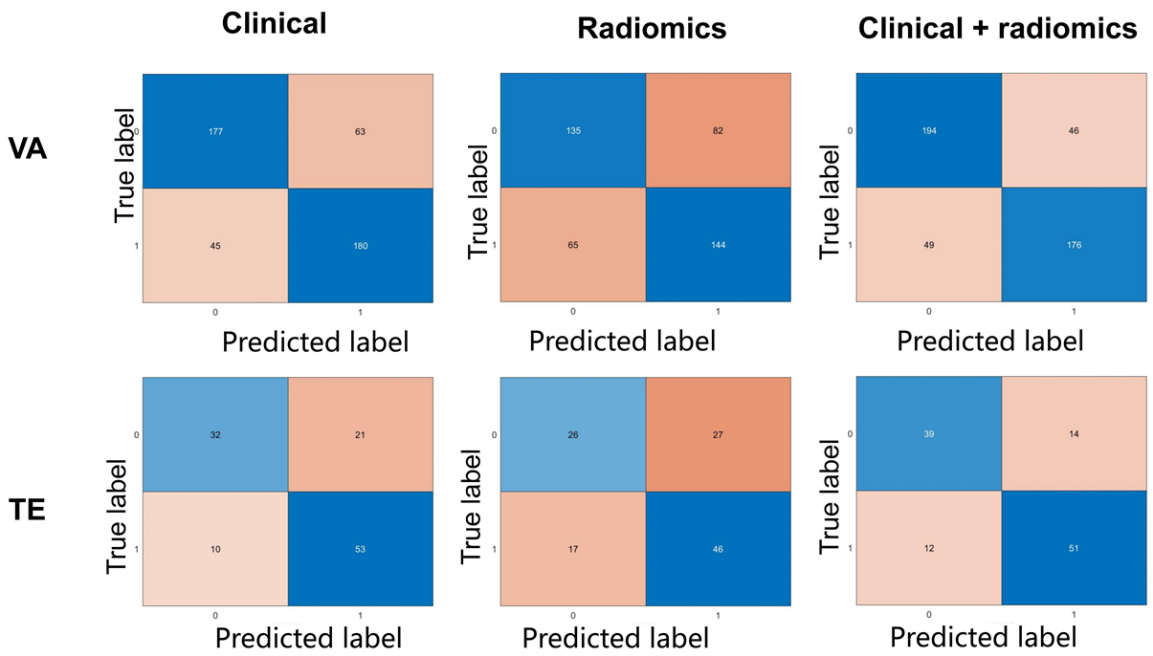

Figure 8. Confusion matrices of different models for predicting microvascular invasion (MVI). The upper panel shows the confusion matrices of the clinical model, radiomics model, and combined clinical-radiomics model in the cross-validation set (VA), and the lower panel shows the corresponding confusion matrices in the independent test set (TE). The horizontal axis represents the predicted class, and the vertical axis represents the true class. Overall, the three models showed distinct classification performance across the two datasets, and the combined model achieved the best overall classification performance in the independent test set.

the best overall predictive performance for both endpoints. These findings support the concept that postoperative recurrence and invasive behavior in HCC are not determined by a single dimension of tumor biology, but rather reflect the combined influence of tumor aggressiveness, tumor microenvironment remodeling, and host systemic condition [26].

A key finding of the present study was the substantial incremental value of radiomics for predicting 1-year recurrence. In the independent test set, the radiomics model performed better than the clinical model, while the combined model yielded the best overall discrimination. This pattern is biologically plausible. Early recurrence after curative hepatectomy is widely regarded as a manifestation of aggressive preexisting tumor biology, such as occult micrometastatic disease, early vascular spread, or residual microscopic lesions present at the time of surgery. These processes are closely linked to intratumoral heterogeneity, which may not be adequately reflected by routine visual assessment alone. Radiomics offers a quantitative means of capturing subtle differences in gray-level distribution, texture, and spatial complexity, and previous studies have reported associations between imaging-derived features and recurrence risk as well as adverse pathological characteristics in HCC [27]. Our findings are consistent with these previous radiomics studies and further suggest that a multimodal ultrasound-based strategy can provide clinically useful preoperative information without reliance on CT- or MRI-based workflows. Thus, ultrasound-based radiomics may serve as a practical approach for capturing clinically relevant tumor heterogeneity associated with early postoperative relapse.

The significant conventional ultrasound and elastography variables identified in the recurrence analysis are also in line with current understanding of aggressive HCC phenotypes. In our cohort, larger tumor size, irregular tumor margin, abnormal vascularity, and higher stiffness-related parameters were associated with recurrence. Larger tumors and irregular margins are commonly regarded as indicators of infiltrative growth and structural disorganization, whereas increased vascular signals may

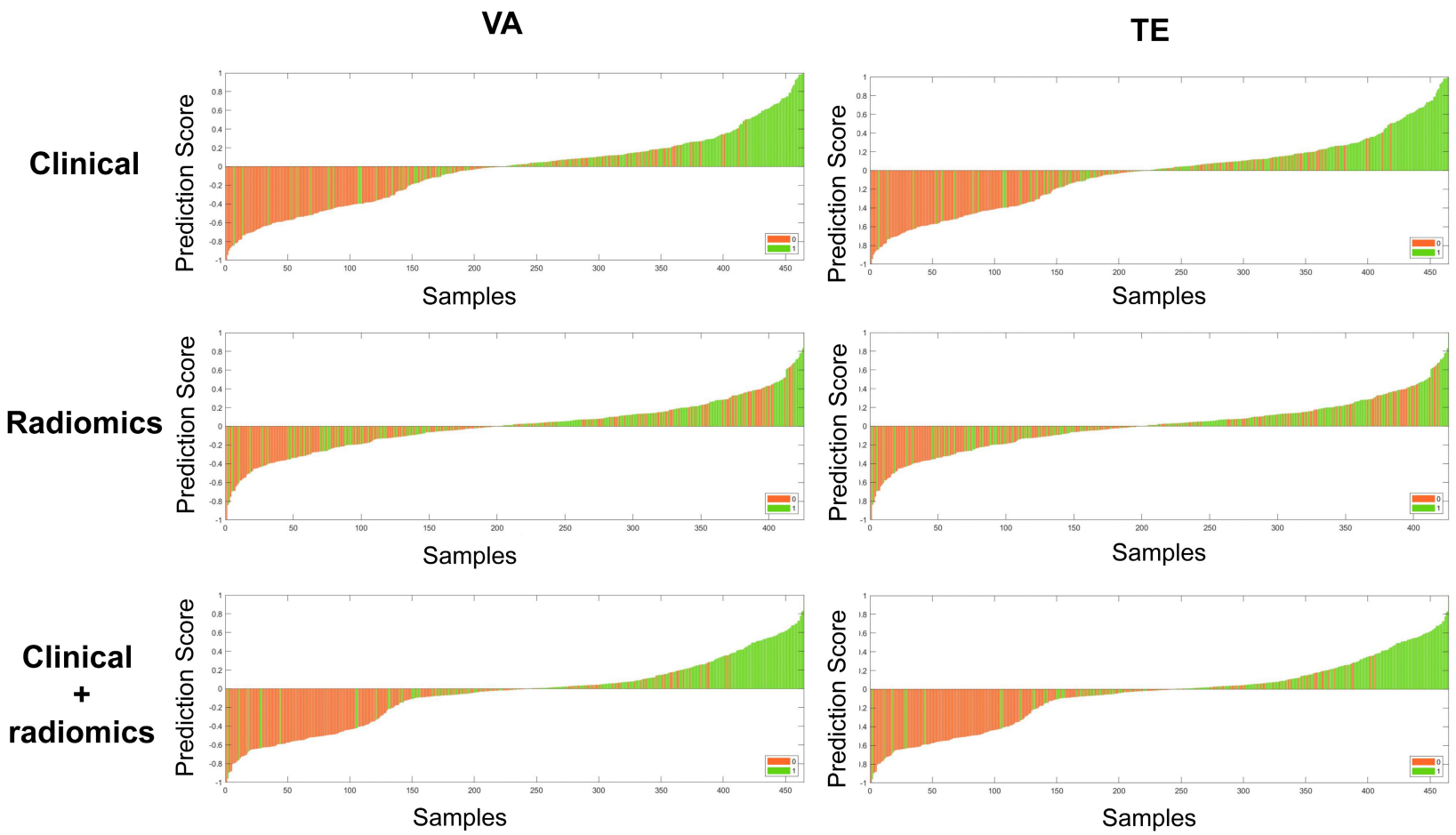

Figure 9. Distribution of predictive scores of different models for microvascular invasion (MVI). The left column shows the cross-validation set (VA), and the right column shows the independent test set (TE). From top to bottom, the panels present the predictive score distributions of the clinical model, radiomics model, and combined clinical-radiomics model, respectively. The horizontal axis represents the samples, the vertical axis represents the predictive score, and different colors indicate different true classes.

reflect angiogenesis, vascular remodeling, or altered intratumoral perfusion [6, 7]. In addition, shear wave elastography-derived parameters, such as mean and maximum shear wave velocity, may reflect tissue stiffness heterogeneity caused by fibrosis, extracellular matrix remodeling, increased cellular density, and stromal reaction [28-30]. Taken together, these features likely represent an imaging phenotype associated with enhanced invasive potential and increased risk of postoperative recurrence.

Compared with recurrence prediction, the pattern observed for MVI prediction was different. In this part of the analysis, the clinical model already showed relatively good discrimination, whereas the radiomics-only model was less effective. Even so, incorporating radiomics features into the clinical model led to additional improvement in predictive performance. This pattern suggests that, for MVI, routinely available host-related and laboratory variables may capture a substantial part of the baseline risk, whereas radiomics contributes supplementary rather than primary discriminative information. Prior CT- and MRI-based radiomics studies have already shown that imaging heterogeneity can be used to predict MVI before surgery [13, 14]. Likewise, earlier ultrasound studies have indicated that conventional sonographic findings and shear wave elastography-derived parameters may also be helpful for preoperative identification of MVI [8]. Our findings are generally consistent with these reports, but further suggest that, within an ultrasound-based framework, MVI prediction may benefit most from combining radiomics with host nutritional-inflammatory-coagulation information rather than relying on imaging features alone.

Another important observation is the contribution of nutritional and inflammatory indicators to both endpoints, particularly to MVI prediction. Variables such as prognostic nutritional index (PNI) [31], albumin, CONUT score [32], and neutrophil-to-lymphocyte ratio (NLR) [33] have been repeatedly associated with prognosis, recurrence, and postoperative outcomes in HCC [34]. Their value in our models is therefore consistent with prior evidence. From a mechanistic perspective, low albumin-related nutritional indices may reflect impaired hepatic synthetic reserve, chronic inflammation, oxidative stress, and reduced tolerance to tumor-associated metabolic burden. Composite nutritional indicators such as PNI and CONUT additionally incorporate lymphocyte-related information and may therefore reflect the balance between nutritional reserve and antitumor immune surveillance. A low PNI or high CONUT score may be associated with reduced immune competence, persistent systemic inflammation, and a tumor-promoting microenvironment, which in turn may facilitate invasive behavior, microvascular spread, and early postoperative recurrence. From a biological perspective, hypoalbuminemia and poor nutritional status may reflect impaired hepatic synthetic function, chronic systemic inflammation, and reduced immune competence, whereas elevated NLR is widely regarded as a marker of tumor-promoting inflammatory activation and immune imbalance [35, 36]. These findings support the view that recurrence and invasive behavior in HCC are shaped not only by tumor-centered pathological features, but also by the metabolic, nutritional-inflammatory status, and immune context of the host [37, 38].

From a mechanistic standpoint, the present results are also compatible with current models of HCC progression. MVI has been linked to epithelial-mesenchymal transition, extracellular matrix remodeling, metabolic reprogramming, immune suppression, and adaptation of the vascular niche [6, 26, 39]. Similarly, early postoperative recurrence reflects a complex biological process involving metastatic dissemination, immune evasion, stromal interaction, and treatment resistance [10, 37, 38, 40]. This mechanistic framework may help explain why radiomics contributed more substantially to recurrence prediction, whereas host-related clinical variables carried a stronger baseline signal for MVI prediction in the present study. Recent molecular studies have further highlighted the roles of tumor-associated neutrophils, macrophages, lysosomal-autophagic pathways, ferroptosis resistance, and EMT-related signaling in shaping aggressive HCC phenotypes [7, 37]. Although molecular validation was not incorporated into the present model, the performance pattern observed for ultrasound radiomics and nutrition-related indicators is consistent with these biology-driven frameworks. In this context, imaging-derived and host-related biomarkers may serve as

clinically accessible surrogates for deeper molecular programs that are otherwise difficult to measure preoperatively.

The present study also has potential translational significance. Compared with CT- or MRI-based radiomics strategies, ultrasound-based assessment is more accessible, less costly, and easier to integrate into routine hepatobiliary practice, particularly in scenarios requiring repeated evaluation or perioperative monitoring. Elastography can be incorporated into standard liver ultrasound workflows with relatively limited additional burden, and previous studies have already suggested its value in the diagnosis and prognostic assessment of HCC. Accordingly, the multimodal ultrasound-based strategy proposed here may represent a more feasible approach for real-world clinical implementation, especially in centers where large-scale cross-sectional radiomics pipelines are less practical.

Several limitations of this work should be acknowledged. First, this was a retrospective single-center study, and the generalizability of the proposed models requires validation in external multicenter cohorts. Second, ultrasound is inherently operator-dependent, and the reproducibility of the models across different ultrasound platforms, acquisition settings, and segmentation procedures warrants further investigation. Third, formal evaluation of model calibration and clinical utility, including calibration curve analysis and decision curve analysis (DCA), was not performed in the present study. Therefore, the clinical net benefit and decision-making value of the proposed models remain to be established. In addition, the absence of external validation further limits the generalizability and translational applicability of the current models. Future prospective multicenter studies are warranted to comprehensively assess model calibration, clinical net benefit, and real-world utility. Fourth, although ROI delineation was performed under a two-reader consensus-based workflow and image quality control criteria were applied during data selection, formal quantitative reproducibility assessment of radiomics features, such as intraobserver and interobserver intraclass correlation coefficient (ICC) analysis, was not performed, which may affect the robustness of feature stability. Finally, the present study focused on conventional ultrasound and elastography; future work should investigate whether contrast-enhanced ultrasound and more biologically interpretable multimodal strategies, as well as integration with molecular profiling and multi-omics data, can further improve predictive performance and biological interpretability.

Conclusions

In patients with HCC undergoing curative hepatectomy, a combined model integrating conventional ultrasound, elastography-derived radiomics, and clinical nutritional indicators demonstrated favorable performance for preoperative prediction of both 1-year recurrence and MVI. The contribution of radiomics was more prominent for early recurrence, whereas clinical indicators showed stronger predictive value for MVI. This multimodal ultrasound-based strategy provides a proof-of-concept framework for individualized risk stratification in HCC.

Disclosure of conflict of interest

None.

Address correspondence to: Yiran Li, Department of Ultrasound Diagnosis and Therapy, Eastern Hepatobiliary Surgery Hospital, The Third Affiliated Hospital of Naval Medical University, Shanghai 200438, China. E-mail: liyiranehsh@sina.com; Fengfeng Mo, Department of Nutrition and Food Hygiene, Naval Medical University, Shanghai 200433, China. E-mail: mofengfeng@smmu.edu.cn

References

[1] He Y, Luo L, Shan R, Qian J, Cui L, Wu Z, Tu S, Zhang W, Lin W, Tang H, Huang Z, Li Z, Mao S, Li H, Hu Z, Liu L, Shen W, He K and Li Y. Development and validation of a nomogram for predicting postoperative early relapse and survival in hepatocellular carcinoma. J Natl Compr Canc Netw 2023; 22: e237069.

[2] Xia F, Yan J, Liu X, Huang Z, Qiu Z, Zhang Q, Wu Z, Huang Z, Wei R, Lin L, Liu L, Han S, Yuan Y, Yin H, Xia G, Wan Y, Xiao S, Li J, Zhou G, Xia X, Sun H, Wang S, Zheng J, Gao H, Zheng J, Ren L, Mo A, Fu J, Ye L, Ruan S, Wang Y, Chen X, Cheng Q, Zhang B and Zhu P. A novel pathologic scoring system for predicting postoperative recurrence in BCLC stage 0-A hepatocellular carcinoma patients: a nationwide multicenter study. Sci China Life Sci 2026; 69: 611-621.

[3] Wang H, Liu R, Mo H, Li R, Lian J, Liu Q and Han S. A novel nomogram predicting the early recurrence of hepatocellular carcinoma patients after R0 resection. Front Oncol 2023; 13: 1133807.
[4] Liu ZH, Chai ZT, Feng JK, Hou YC, Zhang XP, Chen ZH, Xiang YJ, Guo WX, Shi J and Cheng SQ. A reasonable identification of the early recurrence time based on microvascular invasion for hepatocellular carcinoma after R0 resection: a multicenter retrospective study. Cancer Med 2023; 12: 10294-10302.
[5] Zhang ZH, Jiang C, Qiang ZY, Zhou YF, Ji J, Zeng Y and Huang JW. Role of microvascular invasion in early recurrence of hepatocellular carcinoma after liver resection: a literature review. Asian J Surg 2024; 47: 2138-2143.
[6] Niu ZS, Wang WH and Niu XJ. Recent progress in molecular mechanisms of postoperative recurrence and metastasis of hepatocellular carcinoma. World J Gastroenterol 2022; 28: 6433-6477.
[7] Liu L, Qin S, Lin K, Xu Q, Yang Y, Cai J, Zeng Y, Yuan S, Xiang B, Lau WY and Zhou W. Development and comprehensive validation of a predictive prognosis model for very early HCC recurrence within one year after curative resection: a multicenter cohort study. Int J Surg 2024; 110: 3401-3411.
[8] Jiang D, Qian Y, Tan BB, Zhu XL, Dong H and Qian R. Preoperative prediction of microvascular invasion in hepatocellular carcinoma using ultrasound features including elasticity. World J Gastrointest Surg 2023; 15: 2042-2051.
[9] Wang Y, Zhu GQ, Yang R, Wang C, Qu WF, Chu TH, Tang Z, Yang C, Yang L, Zhou CW, Miao GY, Liu WR, Shi YH and Zeng MS. Deciphering intratumoral heterogeneity of hepatocellular carcinoma with microvascular invasion with radiogenomic analysis. J Transl Med 2023; 21: 734.
[10] Ding W, Wu J, Dou J, Liu F, Han Z, Yu J and Liang P. Biologically explicable multimodal model predicting local tumor progression and tumor invasiveness of hepatocellular carcinoma. Hepatology 2026; [Epub ahead of print].
[11] Bo Z, Song J, He Q, Chen B, Chen Z, Xie X, Shu D, Chen K, Wang Y and Chen G. Application of artificial intelligence radiomics in the diagnosis, treatment, and prognosis of hepatocellular carcinoma. Comput Biol Med 2024; 173: 108337.
[12] Wakabayashi T, Ouhmich F, Gonzalez-Cabrera C, Felli E, Saviano A, Agnus V, Savadjiev P, Baumert TF, Pessaux P, Marescaux J and Gallix B. Radiomics in hepatocellular carcinoma: a quantitative review. Hepatol Int 2019; 13: 546-559.
[13] Xia TY, Zhou ZH, Meng XP, Zha JH, Yu Q, Wang WL, Song Y, Wang YC, Tang TY, Xu J, Zhang T, Long XY, Liang Y, Xiao WB and Ju SH. Predicting microvascular invasion in hepatocellular carcinoma using CT-based radiomics model. Radiology 2023; 307: e222729.
[14] Xie XY and Chen R. Research progress of MRI-based radiomics in hepatocellular carcinoma. Front Oncol 2025; 15: 1420599.
[15] Zhang Y, Chen J, Yang C, Dai Y and Zeng M. Preoperative prediction of microvascular invasion in hepatocellular carcinoma using diffusion-weighted imaging-based habitat imaging. Eur Radiol 2024; 34: 3215-3225.
[16] Mitrea DA, Brehar R, Nedevschi S, Lupsor-Platon M, Socaciu M and Badea R. Hepatocellular carcinoma recognition from ultrasound images using combinations of conventional and deep learning techniques. Sensors (Basel) 2023; 23: 2520.
[17] Yao Z, Dong Y, Wu G, Zhang Q, Yang D, Yu JH and Wang WP. Preoperative diagnosis and prediction of hepatocellular carcinoma: radiomics analysis based on multi-modal ultrasound images. BMC Cancer 2018; 18: 1089.
[18] Mohebbi A, Mohammadzadeh S, Mohebbi S, Mohammadi A and Tavangar SM. Diagnostic performance of ultrasound elastography in differentiating hepatocellular carcinoma and intrahepatic cholangiocarcinoma: a systematic review and meta-analysis. Abdom Radiol (NY) 2025; 50: 633-645.
[19] Jiang D, Ren J, Qian Y, Gu Y, Wang R, Yu H, Dong H, Chen D, Chen Y, Jiang H and Li Y. Prediction models after hepatectomy for hepatocellular carcinoma-based ultrasonic radiomics: an observational study. Eur J Med Res 2025; 30: 722.
[20] Wang W, Wu SS, Zhang JC, Xian MF, Huang H, Li W, Zhou ZM, Zhang CQ, Wu TF, Li X, Xu M, Xie XY, Kuang M, Lu MD and Hu HT. Preoperative pathological grading of hepatocellular carcinoma using ultrasomics of contrast-enhanced ultrasound. Acad Radiol 2021; 28: 1094-1101.
[21] Ruiz-Margáin A, Román-Calleja BM, Moreno-Guillén P, González-Regueiro JA, Kúsulas-Delint D, Campos-Murguía A, Flores-García NC and Macías-Rodríguez RU. Nutritional therapy for hepatocellular carcinoma. World J Gastrointest Oncol 2021; 13: 1440-1452.
[22] Tanriverdi O. A discussion of serum albumin level in advanced-stage hepatocellular carcinoma: a medical oncologist's perspective. Med Oncol 2014; 31: 282.
[23] Garrido A and Djouder N. Cirrhosis: a questioned risk factor for hepatocellular carcinoma. Trends Cancer 2021; 7: 29-36.

[24] Chen KL, Qiu YW, Yang M, Wang T, Yang Y, Qiu HZ, Sun T and Wang WT. Prognostic value of preoperative systemic immune-inflammation index/albumin for patients with hepatocellular carcinoma undergoing curative resection. World J Gastroenterol 2024; 30: 5130-5151.
[25] Takagi K, Domagala P, Polak WG, Buettner S and Ijzermans JNM. Prognostic significance of the controlling nutritional status (CONUT) score in patients undergoing hepatectomy for hepatocellular carcinoma: a systematic review and meta-analysis. BMC Gastroenterol 2019; 19: 211.
[26] Huang H, Wu F, Yu Y, Xu B, Chen D, Huo Y and Li S. Multi-transcriptomics analysis of microvascular invasion-related malignant cells and development of a machine learning-based prognostic model in hepatocellular carcinoma. Front Immunol 2024; 15: 1436131.
[27] Guo D, Gu D, Wang H, Wei J, Wang Z, Hao X, Ji Q, Cao S, Song Z, Jiang J, Shen Z, Tian J and Zheng H. Radiomics analysis enables recurrence prediction for hepatocellular carcinoma after liver transplantation. Eur J Radiol 2019; 117: 33-40.
[28] Vestito A, Dajti E, Cortellini F, Montagnani M, Bazzoli F and Zagari RM. Can liver ultrasound elastography predict the risk of hepatocellular carcinoma recurrence after radiofrequency ablation? A systematic review and meta-analysis. Ultraschall Med 2023; 44: e139-e147.
[29] Gu JH, Zhu L and Jiang TA. Quantitative ultrasound elastography methods in focal liver lesions including hepatocellular carcinoma: from diagnosis to prognosis. Ultrasound Q 2021; 37: 90-96.
[30] Jiang D, Qian Y, Gu YJ, Wang R, Yu H, Dong H, Chen DY, Chen Y, Jiang HZ, Tan BB, Peng M and Li YR. Predicting hepatocellular carcinoma: a new non-invasive model based on shear wave elastography. World J Gastroenterol 2024; 30: 3166-3178.
[31] Zhang L, Ma W, Qiu Z, Kuang T, Wang K, Hu B and Wang W. Prognostic nutritional index as a prognostic biomarker for gastrointestinal cancer patients treated with immune checkpoint inhibitors. Front Immunol 2023; 14: 1219929.
[32] Liu R, Ji L, Zhang C, Ye J, Li X, Ma W, Yu J and Wang W. Clinical value of controlling nutritional status scores in patients with hepatocellular carcinoma. Front Nutr 2025; 12: 1598463.
[33] Mouchli M, Reddy S, Gerrard M, Boardman L and Rubio M. Usefulness of neutrophil-to-lymphocyte ratio (NLR) as a prognostic predictor after treatment of hepatocellular carcinoma. Ann Hepatol 2021; 22: 100249.
[34] Ji F, Liang Y, Fu S, Chen D, Cai X, Li S, Peng B, Liang L and Hua Y. Prognostic value of combined preoperative prognostic nutritional index and body mass index in HCC after hepatectomy. HPB (Oxford) 2017; 19: 695-705.
[35] Jin W, Jiang S, Chen A and Chen Y. Effect of preoperative malnutrition based on albumin and BMI on hepatocellular carcinoma surgery and prediction of risk factors of complications. J Gastrointest Cancer 2024; 55: 511-518.
[36] Liang Y, Zhang Z, Zhong D, Lai C, Dai Z, Zou H, Feng T, Shang J, Shi Y and Huang X. The prognostic significance of inflammation-immunity-nutrition score on postoperative survival and recurrence in hepatocellular carcinoma patients. Front Oncol 2022; 12: 913731.
[37] Yang D, Zhou Y, Zhang Y, Su Y, Shen J, Yu B, Zhao K and Ding Y. Comprehensive analysis of scRNA-Seq and bulk RNA-Seq data reveals dynamic changes in tumor-associated neutrophils in the tumor microenvironment of hepatocellular carcinoma and leads to the establishment of a neutrophil-related prognostic model. Cancer Immunol Immunother 2023; 72: 4323-4335.
[38] Yang C, Huang X, Liu Z, Qin W and Wang C. Metabolism-associated molecular classification of hepatocellular carcinoma. Mol Oncol 2020; 14: 896-913.
[39] Tang Y, Xu L, Ren Y, Li Y, Yuan F, Cao M, Zhang Y, Deng M and Yao Z. Identification and validation of a prognostic model based on three MVI-related genes in hepatocellular carcinoma. Int J Biol Sci 2022; 18: 261-275.
[40] Pan J, Zhang M, Dong L, Ji S, Zhang J, Zhang S, Lin Y, Wang X, Ding Z, Qiu S, Gao D, Zhou J, Fan J and Gao Q. Genome-scale CRISPR screen identifies LAPTM5 driving lenvatinib resistance in hepatocellular carcinoma. Autophagy 2023; 19: 1184-1198.

Supplementary Table 1. Categories and composition of radiomics features extracted in this study

Feature category	Subcategory	No. of features	Feature names
Histogram features	Original intensity-based features	18	Energy; histogram entropy; peak value; maximum; mean absolute deviation; mean; median; minimum; intensity range; root mean square; skewness; standard deviation; histogram uniformity; variance; histogram mean; histogram variance; histogram skewness; histogram peak
Texture features	Gray-Level Co-occurrence Matrix (GLCM)	8	Energy; contrast; correlation; homogeneity; variance; sum average; entropy; dissimilarity
Texture features	Gray-Level Run Length Matrix (GLRLM)	13	Short-run emphasis; long-run emphasis; gray-level non-uniformity; run-length non-uniformity; run percentage; low gray-level run emphasis; high gray-level run emphasis; short-run low gray-level emphasis; short-run high gray-level emphasis; long-run low gray-level emphasis; long-run high gray-level emphasis; gray-level variance; run-length variance
Texture features	Gray-Level Size Zone Matrix (GLSZM)	13	Small-zone emphasis; large-zone emphasis; gray-level non-uniformity; zone-size non-uniformity; zone percentage; low gray-level zone emphasis; high gray-level zone emphasis; small-zone low gray-level emphasis; small-zone high gray-level emphasis; large-zone low gray-level emphasis; large-zone high gray-level emphasis; gray-level variance; zone-size variance
Texture features	Neighborhood Gray-Tone Difference Matrix (NGTDM)	5	Coarseness; contrast; busyness; complexity; strength

Note: A total of 18 histogram features and 39 texture features were extracted from each original image. Wavelet decomposition generated eight wavelet sub-band images. Therefore, histogram and texture features were extracted from both the original image and the eight wavelet-transformed images, resulting in 162 histogram features (18×9) and 351 texture features (39×9), respectively. After initial extraction of 513 radiomics features, feature standardization and dimensionality-reduction procedures were sequentially performed before the final selected subset was retained for model construction.

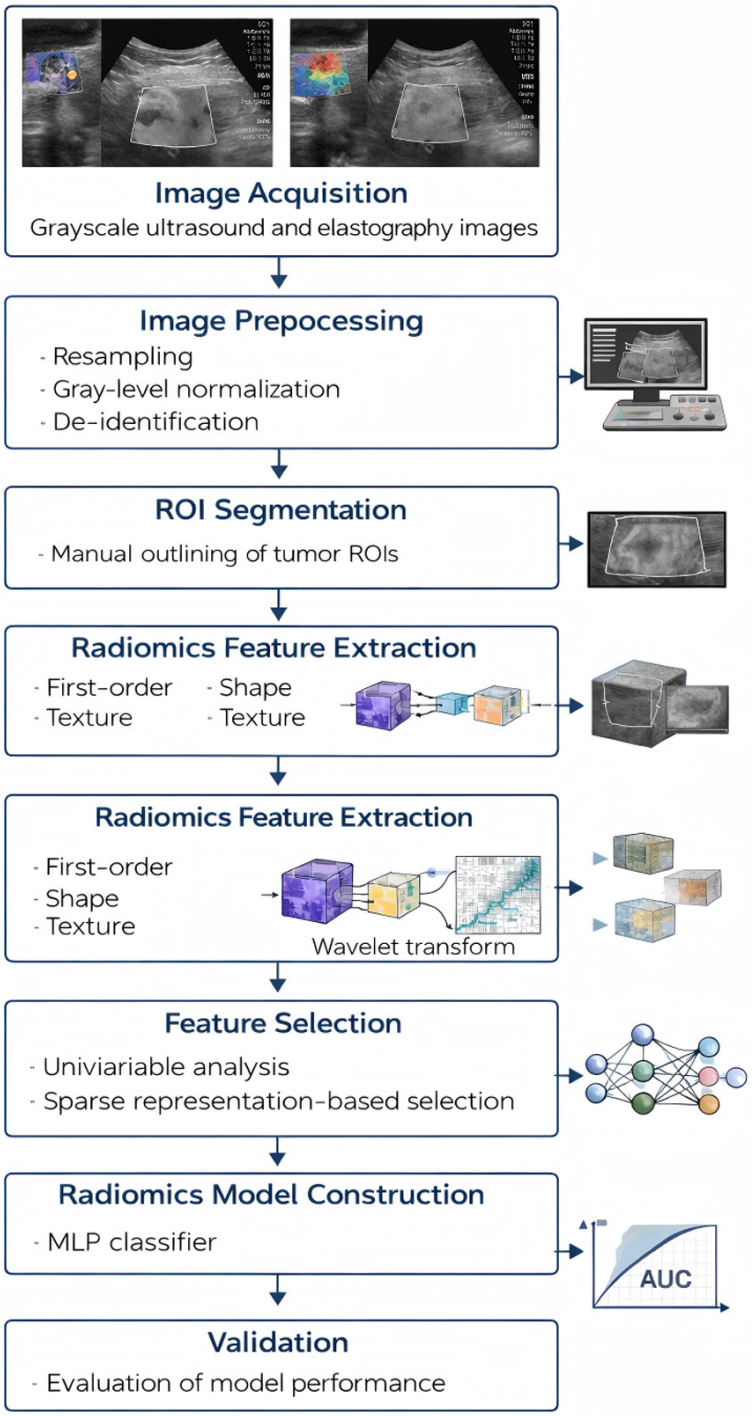

Supplementary Figure 1. Radiomics workflow. The workflow included image acquisition, ROI delineation, image preprocessing, extraction of 513 radiomics features from original and wavelet-transformed images, feature standardization, univariable screening, dimensionality reduction to reduce redundancy and collinearity, and final model construction for endpoint-specific prediction.

Supplementary Table 2. Statistical test results for univariable comparisons between the recurrence and non-recurrence groups

Variable	Statistical test	Test statistic	*P* value
Sex	Chi-square test	$\chi^2 = 0.204$	0.652
Ethnicity	Chi-square test	$\chi^2 = 0.000$	0.999
Age, years	Independent-samples t test	t = 2.695	0.007
Body mass index, kg/m^2	Independent-samples t test	t = -0.418	0.676
Subjective Global Assessment (SGA)	Chi-square test	$\chi^2 = 16.695$	<0.001
Mini Nutritional Assessment (MNA)	Chi-square test	$\chi^2 = 0.602$	0.438
History of tumor	Chi-square test	$\chi^2 = 1.170$	0.279
History of hepatitis	Chi-square test	$\chi^2 = 1.282$	0.258
Antiviral therapy	Chi-square test	$\chi^2 = 0.650$	0.420
Number of tumors	Chi-square test	$\chi^2 = 0.185$	0.667
Surgical approach	Chi-square test	$\chi^2 = 0.040$	0.841
Maximum tumor diameter, mm	Independent-samples t test	t = -3.129	0.002
Peritumoral cirrhosis	Chi-square test	$\chi^2 = 0.091$	0.763
Histopathological subtype	Chi-square test	$\chi^2 = 10.358$	0.035
Tumor differentiation	Chi-square test	$\chi^2 = 1.913$	0.167
Hep-1 expression	Chi-square test	$\chi^2 = 5.939$	0.015
Arginase expression	Chi-square test	$\chi^2 = 3.398$	0.065
GPC-3 expression	Chi-square test	$\chi^2 = 0.020$	0.888
CD34 expression	Chi-square test	$\chi^2 = 0.345$	0.557
Tumor shape	Chi-square test	$\chi^2 = 9.827$	0.002
Echogenicity	Chi-square test	$\chi^2 = 0.075$	0.784
Tumor margin	Chi-square test	$\chi^2 = 7.350$	0.007
Blood flow signal	Chi-square test	$\chi^2 = 12.323$	<0.001
Peritumoral Emax, m/s	Independent-samples t test	t = 0.180	0.857
Peritumoral Emean, m/s	Independent-samples t test	t = -2.057	0.040
Intratumoral Emax, m/s	Independent-samples t test	t = -2.618	0.009
Intratumoral Emean, m/s	Independent-samples t test	t = -2.547	0.011
Total protein, g/L	Independent-samples t test	t = 0.598	0.550
Albumin, g/L	Independent-samples t test	t = 0.399	0.690
Lymphocyte count, ×10^9/L	Independent-samples t test	t = -0.522	0.602
Prognostic Nutritional Index (PNI)	Independent-samples t test	t = 0.221	0.826
Controlling Nutritional Status (CONUT) score	Chi-square test	$\chi^2 = 16.821$	0.002
ALT, U/L	Independent-samples t test	t = 0.902	0.368
AST, U/L	Independent-samples t test	t = -0.347	0.729
GGT, U/L	Independent-samples t test	t = -1.701	0.089
INR	Independent-samples t test	t = -0.502	0.616
PT, s	Independent-samples t test	t = -0.798	0.425
PLT, ×10^9/L	Independent-samples t test	t = -1.329	0.185
Neutrophil count, ×10^9/L	Independent-samples t test	t = -0.657	0.512
NLR, ×10^9/L	Independent-samples t test	t = -0.087	0.931
Glucose, mmol/L	Independent-samples t test	t = 0.033	0.974
AFP, ng/mL	Independent-samples t test	t = -0.305	0.760
CEA, ng/mL	Independent-samples t test	t = -0.209	0.835

Note: χ^2 values were obtained from chi-square tests for categorical variables, and t values were obtained from independent-samples t tests for continuous variables.

Supplementary Table 3. Statistical test results for univariable comparisons between the MVI-positive and MVI-negative groups

Variable	Statistical test	Test statistic	*P* value
Sex	Chi-square test	$\chi^2 = 3.559$	0.059
Ethnicity	Chi-square test	$\chi^2 = 6.840$	0.009
Age, years	Independent-samples t test	t = 1.493	0.136
Body mass index, kg/m^2	Independent-samples t test	t = 1.147	0.252
Subjective Global Assessment (SGA)	Chi-square test	$\chi^2 = 2.961$	0.085
Mini Nutritional Assessment (MNA)	Chi-square test	$\chi^2 = 1.886$	0.170
History of tumor	Chi-square test	$\chi^2 = 0.013$	0.908
History of hepatitis	Chi-square test	$\chi^2 = 1.280$	0.258
Antiviral therapy	Chi-square test	$\chi^2 = 2.305$	0.129
Number of tumors	Chi-square test	$\chi^2 = 3.437$	0.064
Surgical approach	Chi-square test	$\chi^2 = 0.689$	0.406
Maximum tumor diameter, mm	Independent-samples t test	t = 0.647	0.518
Peritumoral cirrhosis	Chi-square test	$\chi^2 = 8.250$	0.004
Histopathological subtype	Chi-square test	$\chi^2 = 180.266$	<0.001
Tumor differentiation	Chi-square test	$\chi^2 = 14.331$	<0.001
Hep-1 expression	Chi-square test	$\chi^2 = 9.208$	0.002
Arginase expression	Chi-square test	$\chi^2 = 2.632$	0.105
GPC-3 expression	Chi-square test	$\chi^2 = 1.618$	0.203
CD34 expression	Chi-square test	$\chi^2 = 6.792$	0.009
Tumor shape	Chi-square test	$\chi^2 = 1.159$	0.282
Echogenicity	Chi-square test	$\chi^2 = 0.069$	0.793
Tumor margin	Chi-square test	$\chi^2 = 3.959$	0.047
Blood flow signal	Chi-square test	$\chi^2 = 0.235$	0.627
Peritumoral Emax, m/s	Independent-samples t test	t = -0.811	0.418
Peritumoral Emean, m/s	Independent-samples t test	t = 0.639	0.523
Intratumoral Emax, m/s	Independent-samples t test	t = -1.351	0.177
Intratumoral Emean, m/s	Independent-samples t test	t = -0.010	0.992
Total protein, g/L	Independent-samples t test	t = -2.072	0.039
Albumin, g/L	Independent-samples t test	t = -4.877	<0.001
Lymphocyte count, ×10^9/L	Independent-samples t test	t = -3.725	<0.001
Prognostic Nutritional Index (PNI)	Independent-samples t test	t = -4.951	<0.001
Controlling Nutritional Status (CONUT) score	Chi-square test	$\chi^2 = 18.271$	0.001
ALT, U/L	Independent-samples t test	t = 0.181	0.857
AST, U/L	Independent-samples t test	t = 1.740	0.082
GGT, U/L	Independent-samples t test	t = 1.798	0.073
INR	Independent-samples t test	t = 2.124	0.034
PT, s	Independent-samples t test	t = 2.225	0.026
PLT, ×10^9/L	Independent-samples t test	t = 0.685	0.494
Neutrophil count, ×10^9/L	Independent-samples t test	t = 0.899	0.369
NLR, ×10^9/L	Independent-samples t test	t = 2.478	0.013
Glucose, mmol/L	Independent-samples t test	t = 1.399	0.162
AFP, ng/mL	Independent-samples t test	t = 0.079	0.937
CEA, ng/mL	Independent-samples t test	t = 0.465	0.642

Note: χ^2 values were obtained from chi-square tests for categorical variables, and t values were obtained from independent-samples t tests for continuous variables.